scientific reports

Check for updates

OPEN

Development of TiO_2-coated YSZ/silica nanofiber membranes with excellent photocatalytic degradation ability for water purification

Jin Young Huh[1,3], Jongman Lee[1,2,3]✉, Syed Zaighum Abbas Bukhari[1], Jang-Hoon Ha[1] & In-Hyuck Song[1,2]

Numerous reports have elucidated that TiO_2 nanoparticles (TiO_2-NPs) exhibit respectable photocatalytic degradation capacities due to their high specific surface areas. However, the current recovery process leads to a loss of TiO_2-NPs; therefore, there is a need to immobilize TiO_2-NPs on the substrate used. Herein, TiO_2-coated yttria-stabilized zirconia/silica nanofiber (TiO_2-coated YSZ/silica NF) was prepared by coating TiO_2 on the surface of YSZ/silica NF using a sol–gel process. The TiO_2 coating layer on the nanofiber surface improved the separation ability of the membrane as well as the photocatalytic degradation ability. The pore size of the TiO_2-coated YSZ/silica NF membrane was less than that of the pristine YSZ/silica NF membrane, and it rejected over 99.6% of the 0.5 µm polymeric particles. In addition, the TiO_2-coated YSZ/silica NF membrane showed excellent adsorption/degradation of humic acid (HA, 88.2%), methylene blue (MB, 92.4%), and tetracycline (TC, 99.5%). Six recycling tests were performed to evaluate the reusability of the TiO_2-coated YSZ/silica NF membrane. The adsorption/degradation efficiency for HA, MB, and TC decreased by 3.7%, 2.8%, and 2.2%, respectively. We thus verified the high separation ability, excellent photocatalytic degradation ability, and excellent reusability of the TiO_2-coated YSZ/silica NF membranes.

Abbreviations

k	Apparent reaction rate constant
BDE	Bond dissociation energy
BET	Brunauer–Emmett–Teller
CFP	Capillary flow porometry
DI	Deionized
DSC	Differential scanning calorimetry
EDS	Energy dispersive spectrometry
C_f	Feeding concentration
FE-SEM	Field-emission scanning electron microscopy
HR-TEM	High-resolution transmission electron microscopy
HA	Humic acid
IEP	Isoelectric point
MB	Methylene blue
MF	Microfiltration
MW	Molecular weight
NPs	Nanoparticles
C_p	Permeate concentration
STEM	Scanning transmission electron microscope

[1]Powder & Ceramics Division, Korea Institute of Materials Science (KIMS), 797 Changwondaero, Seongsangu, Changwon 51508, Republic of Korea. [2]Department of Advanced Materials Engineering, University of Science & Technology (UST), 797 Changwondaero, Seongsangu, Changwon 51508, Republic of Korea. [3]These authors contributed equally: Jin Young Huh and Jongman Lee. ✉email: jmlee@kims.re.kr

SSA	Specific surface area
TC	Tetracycline
TGA	Thermal gravimetric analysis
TTIP	Titanium tetraisopropoxide
TMP	Transmembrane pressure
UF	Ultrafiltration
UV–vis	Ultraviolet–visible
XRD	X-ray diffractometer
YSZ/silica NF	Yttria-stabilized zirconia/silica nanofiber

Electrospinning technology can continuously produce fibers with diameters that range from several nanometers to several micrometers by using a strong electric field. Electrospinning technology has numerous advantages including the provision of (1) a wide selection of materials, (2) a controllable pore structure, (3) high interconnectivity, and (4) the fabrication of complex structures[1–3]. For these reasons, electrospun nanofibers have been applied in various environmental fields such as (1) water and air purification membranes (or filters)[4–6], (2) photocatalysts[7], (3) adsorption[8], and (4) gas sensors[9]. In addition, electrospun nanofibers have been the focus of various studies aimed at the simple manufacture of polymer materials. However, polymer nanofibers cannot be used under harsh conditions due to their (1) poor thermal stability, (2) low chemical durability. To overcome this problem, numerous researchers have developed inorganic nanofibers (such as ceramics) using electrospinning technology[10–14].

In recent decades, the use of photocatalytic nanoparticles (NPs) has been considered as an excellent water purification technology[15–17]. This is because water purification technology using photocatalytic NPs uses light energy, rendering it an eco-friendly technology. Further, photocatalytic degradation processes do not produce harmful substances. In particular, TiO_2 is a representative photocatalyst that is widely applied for environmental purification purposes since it has various advantages such as (1) strong optical adsorption, (2) chemical stability, and (3) low cost. Moreover, TiO_2 NPs have good photocatalytic degradation capacities due to their high specific surface areas. However, there are several challenges faced including difficulties in separating, recovering, and recycling TiO_2-NPs. Moreover, TiO_2-NPs easily form agglomerates due to their high surface energy. This problem requires additional processes such as centrifugation and filtering in the recovery process of TiO_2-NPs[18–20] wherein some TiO_2-NPs are lost. Ultimately, the loss of TiO_2-NPs causes secondary water pollution, low reproducibility, and reduced photocatalytic degradation efficiency[21,22]. To address these disadvantages, various studies have been conducted where TiO_2-NPs are immobilized on various substrates (membranes or filters)[23–28].

We therefore endeavored to immobilize the TiO_2 coating layer on electrospun ceramic nanofibers. Several inorganic materials (especially ceramics) were feasible to avoid the risk of polymeric decomposition by OH radicals and hydrogen peroxide (H_2O_2) that are generated during the photocatalytic reaction[29–31]. The immobilization of TiO_2 coating layers on ceramic NF membranes not only addresses the disadvantages of water purification technology using TiO_2-NPs, but also presents a new direction towards advancing electrospun ceramic NF. Herein, the TiO_2-coated YSZ/silica NF membrane was developed for three purposes: (1) simultaneous separation and photocatalysis, (2) improved photocatalysis (by large surface area), and (3) self-cleaning capability (by photocatalytic degradation). The achievement of these properties requires not only the improvement of both separation and photocatalysis, but also the prevention of TiO_2 loss, which is responsible for the reduction of the photocatalytic efficiency. Accordingly, the morphology, mean/largest pore size, and the specific surface area of the TiO_2-coated YSZ/silica NF membrane were characterized. Furthermore, the gas and pure water permeabilities as well as the rejection rate (%) were analyzed. Lastly, the efficiency of adsorption/photocatalytic degradation was evaluated using major pollutants which represent natural organic matter (HA), organic dye (MB), and antibiotic (TC).

Results and discussion

Characterization of TiO_2-coated YSZ/silica NF. Figure 1 shows the field-emission scanning electron microscopy (FE-SEM) micrographs of pristine YSZ/silica NF and the TiO_2-coated YSZ/silica NF with various TTIP concentrations. The FE-SEM micrographs show the change in the diameter (TiO_2 coating layer plus YSZ/silica NF diameter) depending on the TTIP concentration. This indicates that the TiO_2 coating layer increased as the TTIP concentration raised. For example, the diameters of the YSZ/silica NF and the 0.1 M and 1.0 M TiO_2-coated YSZ/silica NFs were 267 ± 29 nm, 275 ± 31 nm, and 315 ± 28 nm, respectively. The diameter of 1.0 M TiO_2-coated YSZ/silica NF increased by approximately 48 nm (thickness of 24 nm) as compared to that of pristine YSZ/silica NF. An increase in diameter of the TiO_2-coated YSZ/silica NF is able to affect all subsequent membrane characteristics. For example, a reduction in the membrane pore size leads to an increase in the rejection of pollutants, thereby improving the separation capability. The increased TiO_2 coating layer enhances the photocatalytic degradation efficiency. The formation of a TiO_2 coating layer on electrospun nanofibers have also been reported using electrospraying[32] or the sol–gel method[33]. The TiO_2 coating using electrospraying has a disadvantage in that it resulted in TiO_2-NP aggregation which over-coated the electrospun nanofibers.

High-resolution transmission electron microscope (HR-TEM) micrographs and Energy dispersive spectrometry (EDS) spectra confirmed the formation of the TiO_2 coating on YSZ/silica NF. Figure 2A shows the EDS analysis of YSZ/silica NF and 1.0 M TiO_2-coated YSZ/silica NF, confirming the co-existence of zirconium, yttrium, silicon, and oxygen. Titanium was only observed in the 1.0 M TiO_2-coated YSZ/silica NF, indicating that the TiO_2 coating layer was formed. Similarly, Fig. 2B,C show the elemental maps of YSZ/silica NF and 1.0 M TiO_2-coated YSZ/silica NF, respectively. It shows a uniform Ti distribution in the 1.0 M TiO_2-coated YSZ/silica NF, indicating that TiO_2 was homogeneously coated over the entire nanofiber bundle without aggregation.

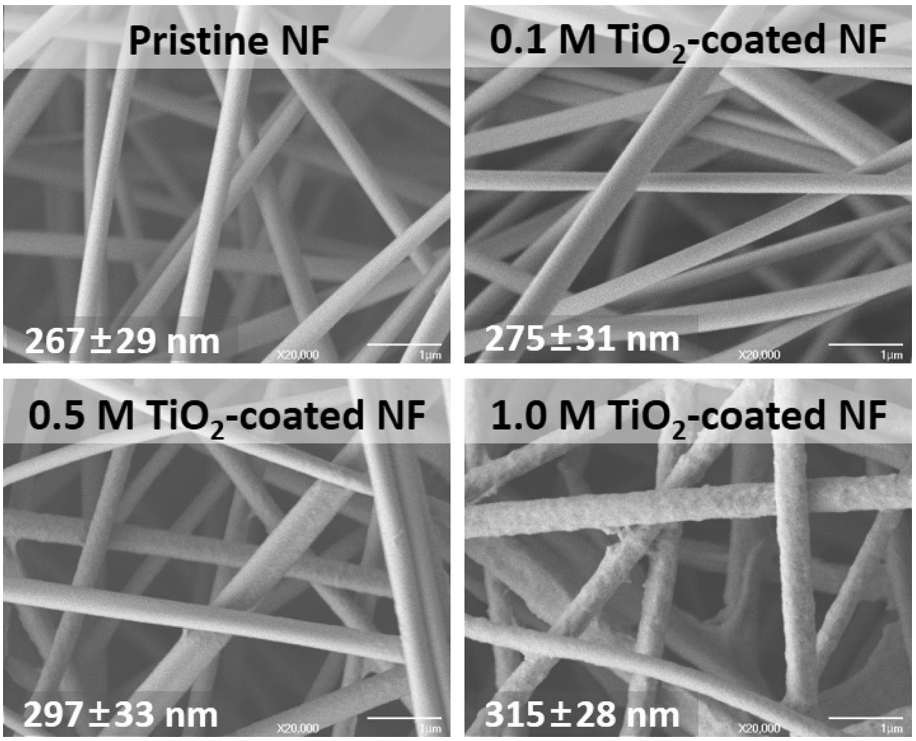

Figure 1. FE-SEM micrographs of YSZ/silica and TiO_2-coated YSZ/silica NF: pristine NF, 0.1 M TiO_2-coated NF, 0.5 M TiO_2-coated NF and 1.0 M TiO_2-coated NF.

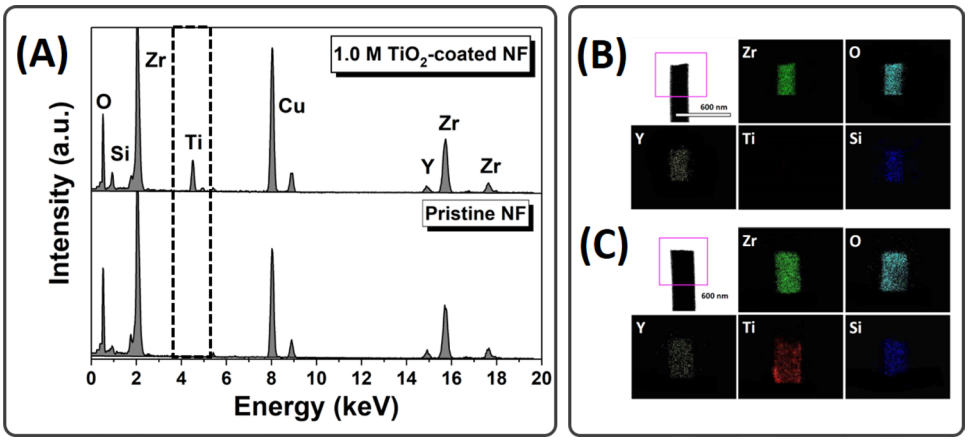

Figure 2. HR-TEM micrographs of YSZ/silica and TiO_2-coated YSZ/silica NF: (**A**) EDS spectra of pristine NF and 1.0 M TiO_2-coated NF and elemental maps of (**B**) pristine NF and (**C**) 1.0 M TiO_2-coated NF.

Figure 3 shows the X-ray diffraction (XRD) diffractogram of both calcined YSZ/silica NF and TiO_2-coated YSZ/silica NF. The diffractogram of the calcined YSZ/silica NF indicates that the stabilized zirconia had a cubic phase (JCPDS No. 01-081-1550). The peaks assigned to zirconia are 30.0°, 34.7° 50.0°, 59.4°, 62.3°, and 73.4° corresponding to the (111), (200), (220), (311), (222), and (400) crystallographic planes, respectively[11,12]. However, new peaks were observed at 25.3°, 37.8°, 53.9°, and 55.1° in TiO_2-coated YSZ/silica NF, which show the crystalline anatase TiO_2 phase (JCPDS No. 89-4320) and crystallographic planes of (101), (004), (105), and (211), respectively[34–36]. In addition, the grain size of the anatase TiO_2 phase in the 0.1 M, 0.5 M, and 1.0 M TiO_2-coated YSZ/silica NF was calculated using Scherrer's equation (16.4 nm, 18.1 nm, and 19.7 nm, respectively). In general, it is known that the grain size of TiO_2 increases with increasing TTIP concentration[37]. This is because the higher TTIP concentration, the faster the growth rate of nuclei than the nucleation rate[38,39].

Thermal gravimetric analysis (TGA) and differential scanning calorimetry (DSC) were conducted on the as-coated and calcined 1.0 M TiO_2-coated YSZ/silica NF in order to analyze the weight loss and changes in heat

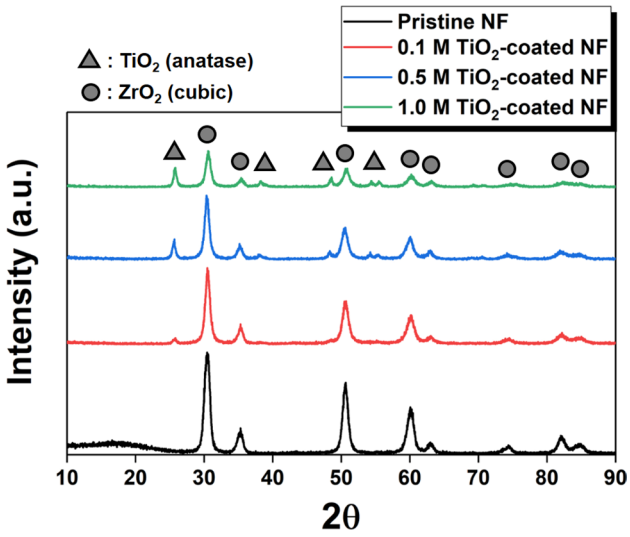

Figure 3. XRD diffractogram of YSZ/silica (pristine) and TiO_2-coated YSZ/silica NF (0.1, 0.5 and 1.0 M TiO_2-coated NF).

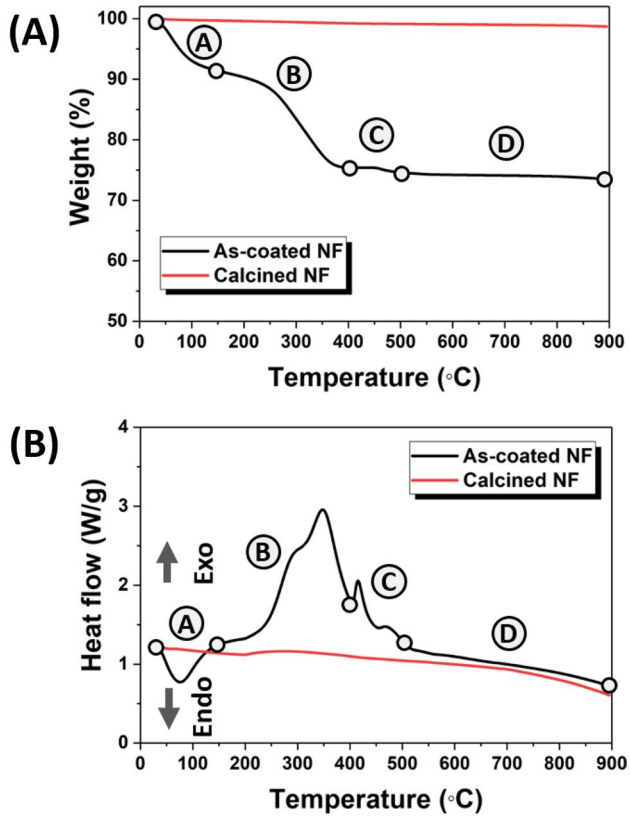

Figure 4. TGA–DSC measurement of as-coated (black line) and calcined (red line) 1.0 M TiO_2-coated NF: (**A**) TGA and (**B**) DSC.

capacity. The pyrolysis of the as-coated 1.0 M TiO_2-coated YSZ/silica NF can be divided into 4 stages, as shown in Fig. 4; Stage A (25–150 ℃), Stage B (150–400 ℃), Stage C (400–500 ℃), and Stage D (500–900 ℃). The TGA curve shows the weight loss of the as-coated 1.0 M TiO_2-coated YSZ/silica NF in Fig. 4A. Stage A showed a weight loss of approximately 9%, which was attributed to the evaporation of water and pyrolysis of residual organic solvents[40,41]. Stage B showed a weight loss of approximately 16% due to the thermal decomposition of the organic residues that occurred during the oxidation of TTIP that transformed it into an amorphous structure[42,43]. In stage

	Pristine NF	0.1 M TiO_2-coated NF	0.5 M TiO_2-coated NF	1.0 M TiO_2-coated NF
SSA (m^2/g)	9.7	10.2	11.6	11.7

Table 1. SSA of YSZ/silica (pristine) and TiO_2-coated YSZ/silica NF.

C, the weight was reduced by approximately 2% due to the thermal decomposition of organics present inside the 1.0 M TiO_2-coated YSZ/silica NF[44,45]. Stage D shows complete removal of all organic compounds and residues, and as a result, no weight change was observed. We analyzed the calcined 1.0 M TiO_2-coated YSZ/silica NF to identify any remaining organic compounds (for reference). No weight loss was observed for the calcined 1.0 M TiO_2-coated YSZ/silica NF in the TGA curve.

The DSC curve shows the heat flow of the as-coated 1.0 M TiO_2-coated YSZ/silica NF, as shown in Fig. 4B. The endothermal peak (76 ℃, in stage A) was due to the evaporation of water, the exothermic peak (350 ℃, in stage B) was caused by the thermal decomposition of organic residue generated during the oxidation of TTIP for transformation into the amorphous structure[46,47]. As shown in stage C, the exothermic peak (417 ℃) is located in the crystallization zone of the anatase TiO_2 phase[48]. The exothermic peak (468 ℃, in stage C) is due to the thermal decomposition of organic compounds present in the 1.0 M TiO_2-coated YSZ/silica NF. The calcined 1.0 M TiO_2-coated YSZ/silica NF showed no change in heat flow as observed in the DSC curve, and this confirmed that no organic compounds were remaining in the sample. If TiO_2-coated YSZ/silica NF is calcined above 500 ℃, the anatase phase can be converted to the rutile or brookite phase[49]. Studies have shown that the anatase phase has better photocatalytic degradation efficiency than the rutile and brookite phases[50–52]. Thus, in our present study, we calcined the samples at 500 ℃ to obtain the anatase TiO_2 phase, which has less recombination potential than the rutile and brookite phases.

Table 1 shows the BET analysis results of YSZ/silica NF and TiO_2-coated YSZ/silica NF. We confirmed the change in the specific surface area (SSA) owing to the formation of the TiO_2 coating layer on YSZ/silica NF. As shown in Table 1, the SSA of YSZ/silica NF is 9.7 m^2/g, and the SSA of TiO_2-coated YSZ/silica NF increased as the TiO_2 coating layer raised from 0.1 M (10.2 m^2/g) to 0.5 M (11.6 m^2/g) and then to 1.0 M (11.7 m^2/g). This is because the increased TiO_2 coating layer on the YSZ/silica NF contributes to expand the SSA. The SSA is a critical factor in adsorption and photocatalysis. The SSA of electrospun ceramic nanofiber membranes have smaller than NPs, but higher than that of conventional ceramic membranes [especially microfiltration (MF) and ultrafiltration (UF) membranes][53,54]. TiO_2-NPs generally have a high SSA, but the problems of aggregation, separation, and recovery hinder their applicability. Although the SSA of TiO_2-coated YSZ/silica NF is relatively smaller than that of the TiO_2-NPs, our research was able to compensate for the drawbacks of TiO_2-NPs.

Figure 5 shows the mean and largest pore size of YSZ/silica NF and TiO_2-coated YSZ/silica NF membranes through the analysis of capillary flow porometry (CFP). The mean pore size of the YSZ/silica NF membrane (0.51 ± 0.05 μm) gradually decreased as the TTIP concentrations increased from 0.1 M (0.48 ± 0.01 μm) to 0.5 M (0.46 ± 0.02 μm) and then to 1.0 M (0.42 ± 0.01 μm) (in Fig. 5A). The largest pore size of the YSZ/silica NF membrane (1.67 ± 0.05 μm) proportionally decreased as the TTIP concentrations increased from 0.1 M (1.48 ± 0.09 μm) to 0.5 M (1.40 ± 0.11 μm) and then to 1.0 M (1.36 ± 0.03 μm) (in Fig. 5B). The mean and large pore size of the TiO_2-coated YSZ/silica NF membranes decreased with increasing TTIP concentration due to the increasing thickness of the nanofibers, which decrease the pore size of the membrane. This reduction in pore size affects the membrane performance.

Membrane performance of TiO_2-coated YSZ/silica NF. Fig. S1 shows the result of gas and pure water permeability for the largest pore size of YSZ/silica NF and TiO_2-coated YSZ/silica NF membranes. In general, gas and pure water permeability increase as the largest pore size of the membrane rises[55,56]. The largest pore size determines the gas and pure water permeability because the fluid flows to the region with least resistance to water mobility corresponding to the largest pore size, which thus determines the gas and pure water permeability[14]. In this study, as shown in Fig. S1, the largest pore size decreases as the TiO_2 coating layer increases. Figure S1(a) shows the gas permeability of YSZ/silica NF membrane (largest pore size: 1.67 μm) is 23.4 ± 1.6 L/cm^2 min bar, and the gas permeability of 1.0 M TiO_2-coated YSZ/silica NF membrane (largest pore size: 1.36 μm) is 11.8 ± 0.9 L/cm^2 min bar. In addition, the pure water permeability of YSZ/silica NF membrane is 46,704 ± 2064 L/m^2 h bar and the pure water permeability of 1.0 M TiO_2-coated YSZ/silica NF membrane is 31,992 ± 3766 L/m^2 h bar, as shown in Fig. S1(b). Thus, the gas and pure water permeability of TiO_2-coated YSZ/silica NF membranes decrease as the largest pore size reduces. Nevertheless, conventional multi-layer ceramic membranes (especially MF and UF membranes) have a large number of closed pores, which decreases the gas and pure water permeability relative to electrospun ceramic nanofiber membranes that have an open pore structure[14,57]. For example, the gas permeability of ceramic membranes is approximately 0.001 L/cm^2 min to 0.004 L/cm^2 min, and the pure water permeability is approximately 250 L/m^2 h to 600 L/m^2 h[58–60]. Therefore, the gas and pure water permeability of the TiO_2-coated YSZ/silica NF membranes is much higher than that of ceramic membranes.

Figure 6 shows the rejection rate (%) of YSZ/silica NF and TiO_2-coated YSZ/silica NF membranes using 0.5 μm polymeric particles. The mean pore size of YSZ/silica NF and TiO_2-coated YSZ/silica NF membranes affected the rejection rate (%) because the mean pore size corresponds to the average index of the pores of the membrane can separate particles larger than the mean pore size. The YSZ/silica NF membrane with the largest mean pore size (0.51 μm) showed the lowest rejection rate (99.6% ± 0.1%), and the 1.0 M TiO_2-coated YSZ/silica NF membrane with the smallest mean pore size (0.42 μm) showed the highest rejection rate (99.9% ± 0.1%). Overall, we confirmed an excellent rejection rate (more than 99.6%) in all the membranes. The difference in the

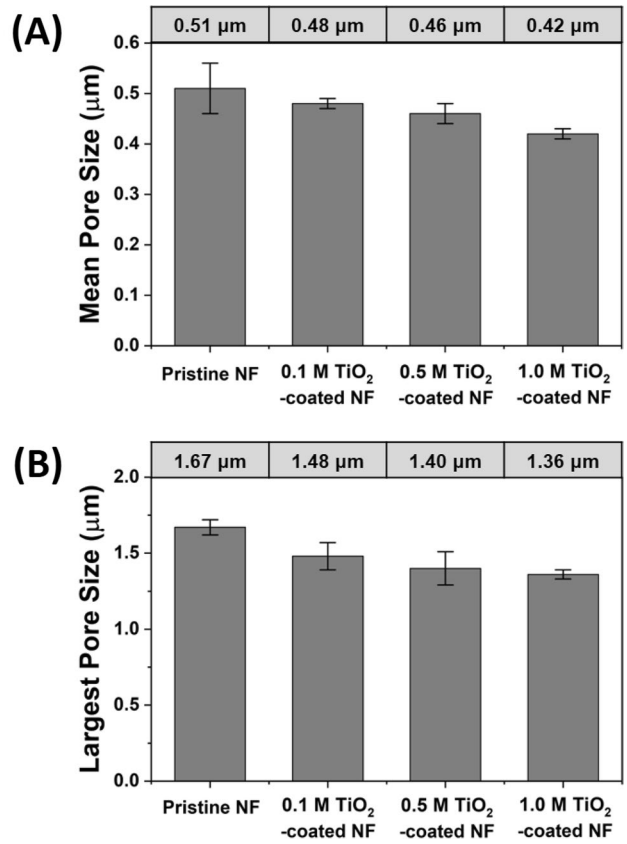

Figure 5. CFP of YSZ/silica (pristine) and TiO_2-coated YSZ/silica NF. (**A**) The mean pore size and (**B**) the largest pore sizes were measured at the concentration of TiO_2 (0, 0.1, 0.5, and 1.0 M).

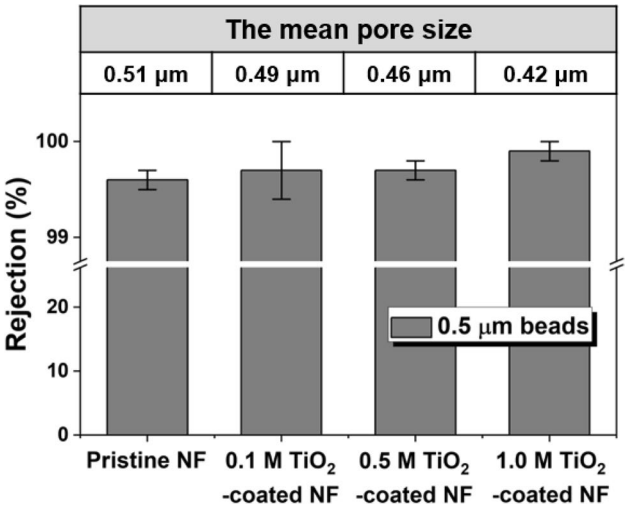

Figure 6. The rejection rate (%) of YSZ/silica (pristine) and TiO_2-coated YSZ/silica NF with 0.5 μm polymeric beads.

rejection rates (%) is due to the mean pore size of TiO_2-coated YSZ/silica NF membranes, which was mostly less than 0.5 μm as shown in Fig. 5A. However, the mean pore size of the YSZ/silica NF membrane was 0.51 μm, which was almost equal to or larger than the diameter of the polymeric particles (0.5 μm), but it was measured at a high rejection rate (%) of approximately 99.6% ± 0.1%. This is observed because the structure of the YSZ/silica NF membrane is so intricately entangled into several layers that the polymeric particles undergo the tortuous pathway through the filtration process[14]. The variation in the rejection rate (%) is directly correlated to a

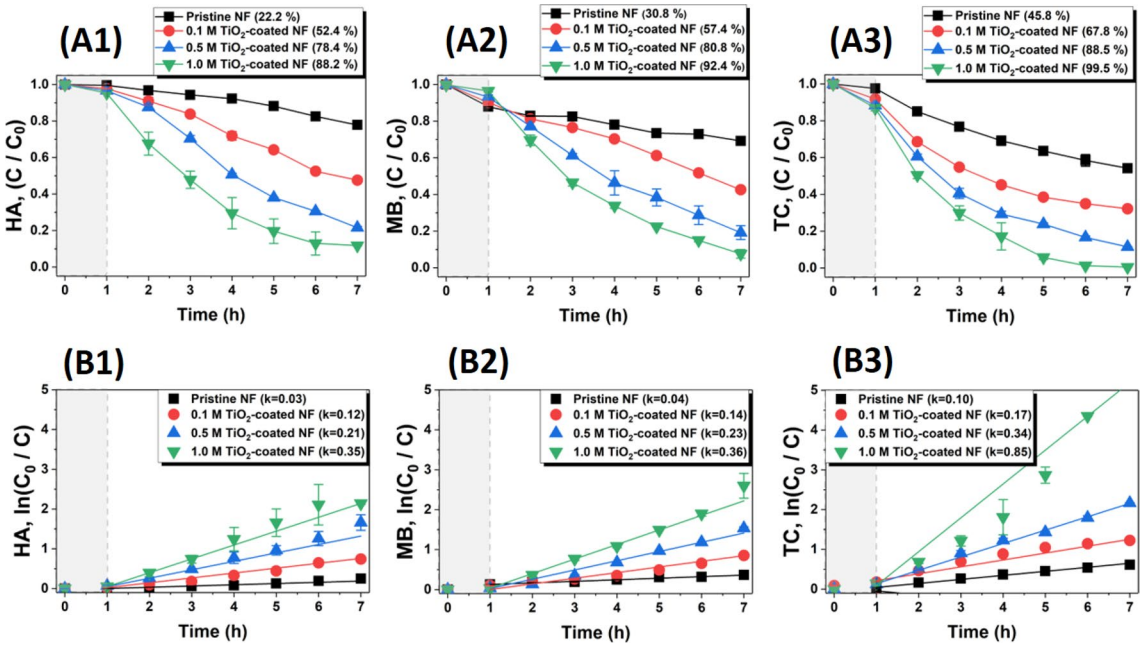

Figure 7. Adsorption/photocatalytic degradation of (**A1**) HA, (**A2**) MB, and (**A3**) TC and apparent reaction rate of (**B1**) HA, (**B2**) MB, and (**B3**) TC by YSZ/silica (pristine) and TiO_2-coated YSZ/silica NF under UV-light irradiation.

difference in the mean pore size of the TiO_2-coated YSZ/silica NF membranes, which gradually decreased due to the increase in the TiO_2 coating layer. In other words, the post-processing for the formation of TiO_2 coating layer on YSZ/silica NF is able to govern the pore size and rejection rate (%).

Photocatalytic degradation of the TiO_2-coated YSZ/silica NF membrane. The photocatalytic degradation of TiO_2-coated YSZ/silica NF was characterized by selecting HA, MB, and TC, which represent natural organic matter, organic dyes, and antibiotics, respectively. In particular, the same pollutant concentration (20 mg/L) was adopted to compare the differences in photocatalytic degradation behavior between pollutants. The pollutant concentrations are likely to be varied for research articles, and the variations are very broad. They are mostly distributed in the range of 5 to 10 mg/L, but a relatively high concentration of 20 mg/L was used herein to demonstrate the great photocatalytic degradation performance of TiO_2-coated YSZ/silica NF[61,62]. That is, we endeavored to accomplish the excellence of our study by using a relatively higher pollutant concentration than the commonly used pollutant concentration. Figure 7 shows the variation in the adsorption/photocatalytic degradation efficiency and the apparent reaction rate of HA, MB, and TC with UV irradiation time of the YSZ/silica NF and TiO_2-coated YSZ/silica NF membranes. As shown in Fig. 7A1, the adsorption/degradation process of HA with the YSZ/silica NF membrane takes a total of 7 h (adsorption: 1 h, degradation: 6 h), and the entire efficiency accounts 22.2% (adsorption: 0.5%, degradation: 21.7%). The adsorption/degradation efficiency of 0.1 M, 0.5 M, and 1.0 M TiO_2-coated YSZ/silica NF membranes were 52.4% ± 0.2% (adsorption: 2.2%, degradation: 50.2%), 78.4% ± 0.8% (adsorption: 3.6%, degradation: 74.8%), and 88.2% ± 0.3% (adsorption: 4.6%, degradation: 83.6%), respectively. In Fig. 7B1, we calculated the apparent reaction rate constant (k) of YSZ/silica NF and the TiO_2-coated YSZ/silica NF membranes using the Langmuir–Hinshelwood rate equation[34,35], which gave the k of YSZ/silica NF membrane for HA as 0.03 h^{-1}, and the k of 0.1 M, 0.5 M, and 1.0 M TiO_2-coated YSZ/silica NF membranes were 0.12 h^{-1}, 0.21 h^{-1}, and 0.35 h^{-1}, respectively. The adsorption/degradation efficiency and apparent reaction rate of HA increased with an increase in the TiO_2 content. We observed similar results for the adsorption/degradation efficiency and apparent reaction rate of MB and TC, as shown in Figs. (A2), (A3), (B2), and (B3). The difference in adsorption/degradation efficiency and the apparent reaction rate of 1.0 M TiO_2-coated NF membrane was HA [88.2% ± 0.3% (adsorption: 4.6%, degradation: 83.6%), k = 0.35 h^{-1}], MB [92.4% ± 2.3% (adsorption: 3.1%, degradation: 89.3%), k = 0.36 h^{-1}], and TC [99.5% ± 0.1% (adsorption: 12.1%, degradation: 87.4%), k = 0.85 h^{-1}]. As a result, the order of the adsorption/degradation pattern of 1.0 M TiO_2-coated NF membrane is HA < MB < TC. This was caused by the difference in the (1) adsorption rate, (2) bond dissociation energy (BDE), and (3) molecular weight (MW) of each pollutant. In general, the interfacial interaction between pollutants and TiO_2 most influences the photocatalytic degradation capability[63]. That is, the lifetime of OH radicals due to the photocatalytic activity of TiO_2 is very short (~ ns), so that only the pollutants adsorbed on the TiO_2 coating layer can be degraded[31]. As shown in Fig. 7, the adsorption rate for each contaminant was HA (4.6%), MB (3.1%), and TC (12.1%) (MB < HA < TC). The adsorption rates varied because the isoelectric point (IEP) was different for each pollutant. Usually, the anatase TiO_2 has an IEP of 7.0, the IEP of HA and TC were 4.7, 4.8, respectively, and MB is a cationic dye[61,64–67]. The pH of each pollutant solution was adjusted to 6.5, and the surface charge of TiO_2 was positive, while HA and TC were negatively charged, and MB was positively charged. As MB has the same surface charge as TiO_2, it has the smallest adsorption rate due to

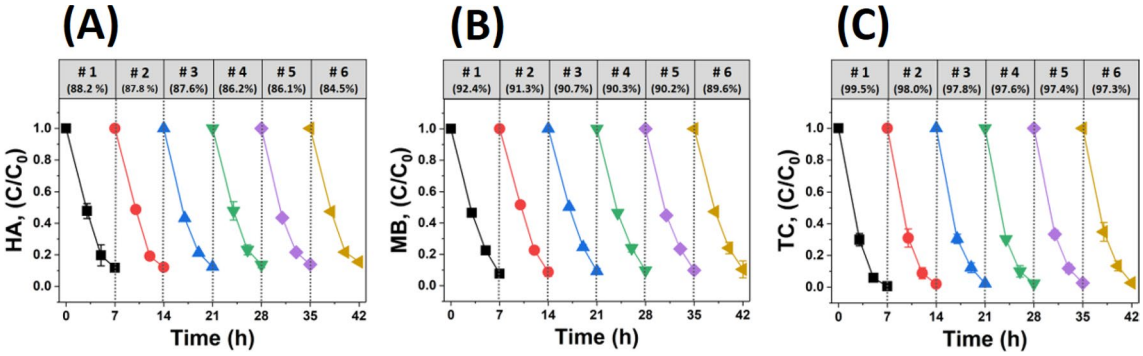

Figure 8. Recycling of (**A**) HA, (**B**) MB, and (**C**) TC by 1.0 M TiO_2-coated YSZ/silica NF under UV-light irradiation.

electrostatic repulsion. HA and TC, which have similar IEPs, have an opposite surface charge from TiO_2, so their adsorption rates are higher than that of MB due to electrostatic attraction. However, the adsorption rate of TC is almost 3 times higher than that of HA, this is because TC is hydrophilic[68–71]. In general, since common metal oxide ceramics are hydrophilic, the hydrophilic TC had a higher adsorption rate than the hydrophobic HA and MB[71,72]. Secondly, each pollutant has different functional groups that are collapsed by OH radical attack. The chemical structure of the pollutants affects photocatalytic degradation behavior, and in particular, the appropriate photocatalytic materials should be selected according to the functional groups. In previous studies[73–77], the functional group cleaved by OH radicals in HA and TC is C = C (BDE: 618.3 ± 15.4 kJ/mol), while that in MB is C = S (BDE: 548.9 kJ/mol). This order of BDE of MB < HA = TC indicates that MB can be better cleaved by OH radicals than HA and TC. Finally, the MW of each pollutant is different. The MW of HA is over 10,000 g/mol, MB is 319.85 g/mol, and TC is 480.90 g/mol (MB < TC ≪ HA). Taken together, TC has the highest adsorption/degradation efficiency, because TC has the highest adsorption rate (12.1%) and relatively smaller MW (480.90 g/mol). MB has the second highest adsorption/degradation efficiency, because the lowest BDE (548.9 kJ/mol) and MW (319.85 g/mol). HA has the least adsorption/degradation efficiency, because relatively smaller adsorption rate (4.6%) and the largest MW (10,000 g/mol).

To compare the adsorption/degradation efficiency and the apparent reaction rate of 1.0 M TiO_2-coated YSZ/silica NF membrane and TiO_2-NPs, we measured adsorption/degradation efficiency and the apparent reaction rate using 5 mg of TiO_2-NPs, as shown in Fig. S3. The adsorption/degradation efficiency and the apparent reaction of the 5 mg TiO_2-NPs was HA [65.4% ± 0.9% (adsorption: 0.8%, degradation: 64.6%), k = 0.17 h^{-1}], MB [67.0% ± 1.1% (adsorption: 4.8%, degradation: 62.2%), k = 0.19 h^{-1}], and TC [98.4% ± 0.1% (adsorption: 2.2%, degradation: 96.2%), k = 0.69 h^{-1}), respectively. It was lower than the adsorption/degradation efficiency and the apparent reaction of 1.0 M TiO_2-coated YSZ/silica NF membrane. This is because the dispersion of TiO_2-NPs varies depending on the shape of the container, and the distance and position from the UV light source are not constant. Moreover, the TiO_2-NPs having high surface energy form agglomerates which can reduce the SSA of the TiO_2-NPs and slowed the reaction of TiO_2-NPs with UV light. As a result, it was verified that the TiO_2-coated YSZ/silica NF membrane had higher adsorption/degradation efficiency than TiO_2-NPs and can effectively photodegrade pollutants from different sources such as HA, MB, and TC.

Figure 8 shows the recycling test for HA, MB, and TC using 1.0 M TiO_2-coated YSZ/silica NF membrane. The adsorption/degradation efficiencies of HA, MB, and TC tend to reduce during a total of six recycling tests. For example, HA decreased by 3.7% (1st cycle:88.2%, 6th cycle: 84.5%), MB by 2.8% (1st cycle: 92.4%, 6th cycle: 89.6%), and TC by 2.2% (1st cycle: 99.5%, 6th cycle: 97.3%). The reason is that the amount of HA, MB, and TC remaining after adsorption and photocatalytic degradation influenced the subsequent recycling test, as shown in Fig. 7. Teixeira et al.[78] experimented on the recycling of $Fe_3O_4/SiO_2/TiO_2$ NPs using MB under UV irradiation for 90 min at each cycle, and they observed a decrease of approximately 14% (1st cycle: 95%, 5th cycle: 81%). In addition, Y. Shi et al.[19] conducted a study on the recycling of palygorskite-supported Cu_2O-TiO_2 composite using TC under Xe lamp irradiation for 240 min at each cycle, and they observed a reduction by approximately 7.57% (1st cycle: 81.45%, 3rd cycle: 73.88%). The main reason for the decrease in adsorption/degradation efficiency in most of the recycling tests are as follows. In each cycle, photocatalytic nanomaterials are more likely to be lost in the recovery process such as filtering and centrifugation, which directly causes the adsorption/degradation efficiency to decrease[34,35]. Meanwhile, in order to minimize photocatalyst loss and prevent secondary environmental pollution, we developed a sol–gel process to tightly secure TiO_2 on the surface of YSZ/silica NF membrane. Even if the photocatalytic recycling test was carried out 6 times in a row for 7 h each time, the decrease in adsorption/degradation efficiency is minimal. Such an excellent reusability is one of the greatest advantages of our study.

Conclusions

In this study, TiO_2-coated YSZ/silica NF was successfully developed by forming a TiO_2 coating layer on the surface of YSZ/silica NF. This study mainly considered two aspects: (1) the ability to simultaneously perform separation and degradation and (2) improving the efficiency of photocatalytic degradation and imparting self-cleaning functionality. To achieve these goals, the TTIP concentration was controlled accordingly during TiO_2 coating process. As the TTIP concentration increased, the TiO_2 coating layer of the YSZ/silica NF raised. The increasing TiO_2 coating layer reduced the pore size of the membrane, and thus the separation ability of the

TiO_2-coated YSZ/silica NF membrane was improved. Moreover, the TiO_2 coating layer formed was able to efficiently degrade various pollutants with excellent adsorption/photocatalytic degradation. To verify the stability of the formed TiO_2 coating layer, recycling tests were carried out, which confirmed the stability and reusability of TiO_2-coated YSZ/silica NF membranes. In conclusion, we succeeded in developing a stable TiO_2-coated YSZ/silica NF membrane capable of simultaneously separating and photocatalytically degrading HA, MB, and TC, which is expected to play an important role in water purification.

Materials and methods

Fabrication of TiO_2-coated YSZ/silica NF. An electrospinning solution containing 1.6 M zirconium (IV) propoxide solution (Sigma-Aldrich, USA), 8 mol% yttrium (III) nitrate hexahydrate (Sigma-Aldrich, USA), 30 mol% tetraethyl orthosilicate (Sigma-Aldrich, USA), 10 wt% polyvinylpyrrolidone (Sigma-Aldrich, USA), N,N-dimethylformamide (Sigma-Aldrich, USA), and acetic acid (Sigma-Aldrich, USA) was prepared for the fabrication of YSZ/silica NF. The solution was stirred at 30 ℃ until it was clear. Electrospinning of YSZ/silica NF was conducted in a closed chamber system (NanoNC, Republic of Korea) under a controlled relative humidity (40% ± 5%) and temperature (25 ± 2 ℃). The electrospinning solution was placed in a plastic syringe and then ejected through an electrically conducting stainless-steel nozzle (23 G) at a feed rate of 1 ml/h. The applied voltage was 20 kV. The distance between the nozzle tip and the collector was set to 10 cm. The as-spun YSZ/silica nanofibers were dried in a vacuum oven at 30 ℃ for 5 h and then calcined at 800 ℃ for 2 h at a heating rate of 5 ℃/min in air. For TiO_2 coating on the YSZ/silica NF, a TiO_2 sol was prepared with 0.1 M, 0.5 M and 1.0 M titanium tetraisopropoxide (TTIP, Sigma-Aldrich, USA) as the TiO_2 precursor, acetylacetone (Sigma-Aldrich, USA), 2-propanol (Samchun Chemicals, Republic of Korea), acetic acid (Sigma-Aldrich, USA), and deionized (DI) water, which were stirred at 60 ℃ for 5 h. The YSZ/silica NF were submerged in the TiO_2 sol for 5 min under vacuum and then rinsed with 2-propanol in triplicate. The TiO_2-coated YSZ/silica NF were dried overnight in ambient conditions and calcined at 500 ℃ for 1 h at a heating rate of 5 ℃/min in air. Finally, the TiO_2-coated YSZ/silica NF were evaluated with respect to their physicochemical properties, membrane performance, and photocatalytic degradation.

Characterization of TiO_2-coated YSZ/silica NF. The surface morphology was characterized using FE-SEM (JSM-6700, JEOL, Japan) at an accelerating voltage of 5 kV and a magnification of 20,000×. HR-TEM (JEM2100F, JEOL, Japan) was also used for morphological and elemental analysis at an accelerating voltage of 200 kV and a magnification of 150,000× along with EDS (Aztec, OXFORD Instruments, UK). All electron microscope micrographs were analyzed using an image processing software (ImageJ, National Institutes Health, USA) to calculate the average fiber diameter (from more than 30 randomly selected ceramic nanofibers). The crystalline structure was analyzed with XRD (D/Max 2500 V/PC, Rigaku Corporation, Japan) using Cu kα radiation (λ = 1.5406 Å) at 40 kV and 200 mA under the scanning speed of 4°/min and a scan range (2θ) from 10 to 90°. The grain size was calculated using Scherrer's equation[11,79]. The SSA was characterized using the BET (Autosorb-iQ, Quantachrome Instrument, USA) analysis with nitrogen as the adsorbent. TGA and DSC (SDT-Q600, TA Instruments, UK) were conducted within a temperature range of 20 to 900 ℃ at a heating rate of 10 ℃/min in an air atmosphere. The mean pore size and the largest pore size were analyzed using CFP (1200-AEL, Porous Materials, USA). The mean pore size was mainly associated with the rejection (or separation) capacity of the nanofibrous membranes. The largest pore size is more relevant to the air/water permeability (or transport property) of the nanofibrous membranes[14,80].

Membrane performance and photocatalytic degradation of TiO_2-coated YSZ/silica NF. The gas permeability was tested using CFP (1200-AEL, Porous Materials, USA). The measurement was carried out at a pressure of 1.0 bar with air. The pure water permeability was determined using a cross-flow membrane testing system (PHILOS, Republic of Korea). The measurement was conducted at a transmembrane pressure (TMP) of 0.15 bar with a fluid velocity of 2.5 L/min. The rejection rate (%) was analyzed using 0.5 μm polymeric particles (Polysciences, USA). The solution containing polymeric particles was prepared by diluting it with DI water to a concentration of 250 ppm. The contents of feeding concentration (C_f) and that of the permeate concentration (C_p) were measured using ultraviolet–visible (UV–vis) spectroscopy (UV5, Mettler-Toledo GmbH, USA) at a wavelength of 600 nm. The rejection rate (%) was calculated using the following Eq. (1):

$$\text{Rejection rate (\%)} = \left(1 - \frac{C_p}{C_f}\right) \times 100 \quad (1)$$

The adsorption/photocatalytic degradation of the TiO_2-coated YSZ/silica NF was evaluated using three different pollutants containing (1) HA (natural organic matter, Sigma-Aldrich, USA), (2) MB (organic dye, Sigma-Aldrich, USA) and (3) TC (antibiotic, Sigma-Aldrich, USA). The schematic diagram of adsorption/photocatalytic degradation process is described in Fig. S2. The TiO_2-coated YSZ/silica NF membranes (50 mm in diameter) were completely submerged in the pollutant solutions (20 mg/L, pH 6.5) and left in a dark condition for 1 h to reach the adsorption equilibrium. The photocatalytic degradation was initiated using UV irradiation (30 W, 365 nm, Vilber Lourmat, France) for 6 h while the pollutant solutions were constantly shaken to ensure proper mixing. Aliquots were taken at regular time intervals (1 h) to measure the absorbance of pollutant solutions using UV–vis spectroscopy (UV5, Mettler-Toledo GmbH, USA). The specific wavelengths of 254 nm, 663 nm, and 356 nm were adopted to determine the HA, MB, and TC contents, respectively. The rate constant for the photodegradation reaction was determined using Eq. (2):

$$\ln(C_0/C) = kt \quad (2)$$

where, C_0 and C are the concentrations at initial and reaction time t, respectively; k is the apparent reaction rate constant (i.e. pseudo-first-order rate constant). Furthermore, a recycling test of 1.0 M TiO_2-coated YSZ/silica NF membrane was conducted to determine its reusability following the same way as the adsorption/degradation test described above. It was carried out 6 times in a row and reused after washing (with DI water for 1 h) and drying (in a 50 ℃ oven for 4 h) every cycle.

Received: 8 July 2020; Accepted: 30 September 2020
Published online: 20 October 2020

References

1. Hunley, M. T. & Long, T. E. Electrospinning functional nanoscale fibers: A perspective for the future. *Polym. Int.* **57**, 385–389 (2008).
2. Lannutti, J., Reneker, D., Ma, T., Tomasko, D. & Farson, D. Electrospinning for tissue engineering scaffolds. *Mater. Sci. Eng. C* **27**, 504–509 (2007).
3. Zussman, E., Theron, A. & Yarin, A. Formation of nanofiber crossbars in electrospinning. *Appl. Phys. Lett.* **82**, 973–975 (2003).
4. Al-Attabi, R., Dumée, L. F., Kong, L., Schütz, J. A. & Morsi, Y. High efficiency poly (acrylonitrile) electrospun nanofiber membranes for airborne nanomaterials filtration. *Adv. Eng. Mater.* **20**, 1700572 (2018).
5. Xu, J. *et al.* Roll-to-roll transfer of electrospun nanofiber film for high-efficiency transparent air filter. *Nano Lett.* **16**, 1270–1275 (2016).
6. Obaid, M. *et al.* Effective and reusable oil/water separation membranes based on modified polysulfone electrospun nanofiber mats. *Chem. Eng. J.* **259**, 449–456 (2015).
7. Zhang, L. *et al.* Large scaled synthesis of heterostructured electrospun TiO2/SnO2 nanofibers with an enhanced photocatalytic activity. *J. Electrochem. Soc.* **164**, H651–H656 (2017).
8. Liu, Q., Zhong, L.-B., Zhao, Q.-B., Frear, C. & Zheng, Y.-M. Synthesis of Fe3O4/polyacrylonitrile composite electrospun nanofiber mat for effective adsorption of tetracycline. *ACS Appl. Mater. Interfaces.* **7**, 14573–14583 (2015).
9. Kou, X. *et al.* Superior acetone gas sensor based on electrospun SnO_2 nanofibers by Rh doping. *Sens. Actuators B Chem.* **256**, 861–869 (2018).
10. Tang, Y., Liu, Z., Zhao, K. & Fu, S. Positively charged and flexible SiO_2@ZrO_2 nanofibrous membranes and their application in adsorption and separation. *RSC Adv.* **8**, 13018–13025 (2018).
11. Koo, J. Y. *et al.* Controlling the diameter of electrospun Yttria-stabilized zirconia nanofibers. *J. Am. Ceram. Soc.* **99**, 3146–3150 (2016).
12. Mao, X. *et al.* Brittle-flexible-brittle transition in nanocrystalline zirconia nanofibrous membranes. *CrystEngComm* **18**, 1139–1146 (2016).
13. Sun, Y. *et al.* Preparation of fine-grained silica-doped zirconia fibers by electrospinning. *Ceram. Int.* **43**, 12551–12556 (2017).
14. Kim, J., Lee, J., Ha, J.-H. & Song, I.-H. Effect of silica on flexibility of yttria-stabilized zirconia nanofibers for developing water purification membranes. *Ceram. Int.* **45**(14), 17696–17704 (2019).
15. Youssef, Z. *et al.* Dye-sensitized nanoparticles for heterogeneous photocatalysis: Cases studies with TiO_2, ZnO, fullerene and graphene for water purification. *Dyes Pigm.* **159**, 49–71 (2018).
16. Yan, X. *et al.* The interplay of sulfur doping and surface hydroxyl in band gap engineering: Mesoporous sulfur-doped TiO_2 coupled with magnetite as a recyclable, efficient, visible light active photocatalyst for water purification. *Appl. Catal. B* **218**, 20–31 (2017).
17. Zhang, X., Chen, Y., Zhang, S. & Qiu, C. High photocatalytic performance of high concentration Al-doped ZnO nanoparticles. *Sep. Purif. Technol.* **172**, 236–241 (2017).
18. Song, H., Shao, J., He, Y., Liu, B. & Zhong, X. Natural organic matter removal and flux decline with PEG–TiO_2-doped PVDF membranes by integration of ultrafiltration with photocatalysis. *J. Membr. Sci.* **405**, 48–56 (2012).
19. Shi, Y. *et al.* Adsorption and photocatalytic degradation of tetracycline hydrochloride using a palygorskite-supported Cu_2O–TiO_2 composite. *Appl. Clay Sci.* **119**, 311–320 (2016).
20. Reddy, K. R. *et al.* Enhanced photocatalytic activity of nanostructured titanium dioxide/polyaniline hybrid photocatalysts. *Polyhedron* **120**, 169–174 (2016).
21. Zhao, C. *et al.* Advantages of TiO_2/5A composite catalyst for photocatalytic degradation of antibiotic oxytetracycline in aqueous solution: Comparison between TiO_2 and TiO_2/5A composite system. *Chem. Eng. J.* **248**, 280–289 (2014).
22. Rong, X. *et al.* Preparation, characterization and photocatalytic application of TiO_2–graphene photocatalyst under visible light irradiation. *Ceram. Int.* **41**, 2502–2511 (2015).
23. Lombardi, M., Palmero, P., Sangermano, M. & Varesano, A. Electrospun polyamide-6 membranes containing titanium dioxide as photocatalyst. *Polym. Int.* **60**, 234–239 (2011).
24. Daels, N., Radoicic, M., Radetic, M., Van Hulle, S. W. & De Clerck, K. Functionalisation of electrospun polymer nanofibre membranes with TiO_2 nanoparticles in view of dissolved organic matter photodegradation. *Sep. Purif. Technol.* **133**, 282–290 (2014).
25. Geltmeyer, J. *et al.* TiO2 functionalized nanofibrous membranes for removal of organic (micro) pollutants from water. *Sep. Purif. Technol.* **179**, 533–541 (2017).
26. Rahimpour, A., Madaeni, S., Taheri, A. & Mansourpanah, Y. Coupling TiO_2 nanoparticles with UV irradiation for modification of polyethersulfone ultrafiltration membranes. *J. Membr. Sci.* **313**, 158–169 (2008).
27. Bet-Moushoul, E., Mansourpanah, Y., Farhadi, K. & Tabatabaei, M. TiO_2 nanocomposite based polymeric membranes: A review on performance improvement for various applications in chemical engineering processes. *Chem. Eng. J.* **283**, 29–46 (2016).
28. Leong, S. *et al.* TiO_2 based photocatalytic membranes: A review. *J. Membr. Sci.* **472**, 167–184 (2014).
29. Horikoshi, S., Serpone, N., Hisamatsu, Y. & Hidaka, H. Photocatalyzed degradation of polymers in aqueous semiconductor suspensions. 3. Photooxidation of a solid polymer: TiO_2-blended poly (vinyl chloride) film. *Environ. Sci. Technol.* **32**, 4010–4016 (1998).
30. Horikoshi, S., Hidaka, H. & Serpone, N. Photocatalyzed degradation of polymers in aqueous semiconductor suspensions: V. Photomineralization of lactam ring-pendant polyvinylpyrrolidone at titania/water interfaces. *J. Photochem. Photobiol. A Chem.* **138**, 69–77 (2001).
31. Chin, S. S., Chiang, K. & Fane, A. G. The stability of polymeric membranes in a TiO_2 photocatalysis process. *J. Membr. Sci.* **275**, 202–211 (2006).
32. Ramasundaram, S. *et al.* Photocatalytic applications of paper-like poly (vinylidene fluoride)–titanium dioxide hybrids fabricated using a combination of electrospinning and electrospraying. *J. Hazard. Mater.* **285**, 267–276 (2015).
33. Tang, X. *et al.* A simple and innovative route to remarkably enhance the photocatalytic performance of TiO_2: Using micro-meso porous silica nanofibers as carrier to support highly-dispersed TiO_2 nanoparticles. *Microporous Mesoporous Mater.* **258**, 251–261 (2018).

34. An, H.-R. *et al.* Nanoporous hydrogenated TiO_2 photocatalysts generated by underwater discharge plasma treatment for solar photocatalytic applications. *Appl. Catal. B* **211**, 126–136 (2017).
35. An, H.-R. *et al.* Studies on mass production and highly solar light photocatalytic properties of gray hydrogenated-TiO_2 sphere photocatalysts. *J. Hazard. Mater.* **358**, 222–233 (2018).
36. Huh, J. Y. *et al.* Facile, rapid, one-pot synthesis of hydrogenated TiO_2 by using an atmospheric-pressure plasma jet submerged in solution. *Scripta Mater.* **162**, 9–13 (2019).
37. Yazid, S. A., Rosli, Z. M. & Juoi, J. M. Effect of titanium (IV) isopropoxide molarity on the crystallinity and photocatalytic activity of titanium dioxide thin film deposited via green sol–gel route. *J. Mater. Res. Technol.* **8**, 1434–1439 (2019).
38. Jang, H. D. & Jeong, J. The effects of temperature on particle size in the gas-phase production of TiO_2. *Aerosol Sci. Technol.* **23**, 553–560 (1995).
39. Kim, C. S., Nakaso, K., Xia, B., Okuyama, K. & Shimada, M. A new observation on the phase transformation of TiO_2 nanoparticles produced by a CVD method. *Aerosol Sci. Technol.* **39**, 104–112 (2005).
40. Balamurugan, A., Kannan, S. & Rajeswari, S. Evaluation of TiO_2 coatings obtained using the sol–gel technique on surgical grade type 316L stainless steel in simulated body fluid. *Mater. Lett.* **59**, 3138–3143 (2005).
41. Qiu, S. & Kalita, S. J. Synthesis, processing and characterization of nanocrystalline titanium dioxide. *Mater. Sci. Eng. A* **435**, 327–332 (2006).
42. Choi, H., Kim, Y. J., Varma, R. S. & Dionysiou, D. D. Thermally stable nanocrystalline TiO_2 photocatalysts synthesized via sol–gel methods modified with ionic liquid and surfactant molecules. *Chem. Mater.* **18**, 5377–5384 (2006).
43. You, Y. *et al.* Structural characterization and optical property of TiO2 powders prepared by the sol–gel method. *Ceram. Int.* **40**, 8659–8666 (2014).
44. Nagarjuna, R., Roy, S. & Ganesan, R. Polymerizable sol–gel precursor mediated synthesis of TiO_2 supported zeolite-4A and its photodegradation of methylene blue. *Microporous Mesoporous Mater.* **211**, 1–8 (2015).
45. Wu, L., Jimmy, C. Y., Zhang, L., Wang, X. & Ho, W. Preparation of a highly active nanocrystalline TiO_2 photocatalyst from titanium oxo cluster precursor. *J. Solid State Chem.* **177**, 2584–2590 (2004).
46. Xie, H., Zhang, Q., Xi, T., Wang, J. & Liu, Y. Thermal analysis on nanosized TiO_2 prepared by hydrolysis. *Thermochim. Acta* **381**, 45–48 (2002).
47. Ershov, K. S., Kochubei, S. A., Kiselev, V. G. & Baklanov, A. V. Decomposition pathways of titanium isopropoxide Ti (OiPr) 4: New insights from UV-photodissociation experiments and quantum chemical calculations. *J. Phys. Chem. A* **122**, 1064–1070 (2018).
48. Yürüm, A. & Karakaş, G. Synthesis of Na-, Fe-, and Co-promoted TiO_2 multiwalled carbon nanotube composites and their use as a photocatalyst. *Turk. J. Chem.* **41**, 440–454 (2017).
49. Fischer, K. *et al.* Low-temperature synthesis of anatase/rutile/brookite TiO_2 nanoparticles on a polymer membrane for photocatalysis. *Catalysts* **7**, 209 (2017).
50. Li, Z., Cong, S. & Xu, Y. Brookite vs anatase TiO_2 in the photocatalytic activity for organic degradation in water. *ACS Catal.* **4**, 3273–3280 (2014).
51. Gautam, A., Kshirsagar, A., Biswas, R., Banerjee, S. & Khanna, P. K. Photodegradation of organic dyes based on anatase and rutile TiO_2 nanoparticles. *RSC Adv.* **6**, 2746–2759 (2016).
52. Zhang, J., Zhou, P., Liu, J. & Yu, J. New understanding of the difference of photocatalytic activity among anatase, rutile and brookite TiO_2. *Phys. Chem. Chem. Phys.* **16**, 20382–20386 (2014).
53. Panda, P. Ceramic nanofibers by electrospinning technique—A review. *Trans. Indian Ceram. Soc.* **66**, 65–76 (2007).
54. Doh, S. J., Kim, C., Lee, S. G., Lee, S. J. & Kim, H. Development of photocatalytic TiO_2 nanofibers by electrospinning and its application to degradation of dye pollutants. *J. Hazard. Mater.* **154**, 118–127 (2008).
55. Nishiyama, N. & Yokoyama, T. Permeability of porous media: Role of the critical pore size. *J. Geophys. Res. Solid Earth* **122**, 6955–6971 (2017).
56. Alkhudhiri, A., Darwish, N. & Hilal, N. Membrane distillation: A comprehensive review. *Desalination* **287**, 2–18 (2012).
57. Yu, J. *et al.* Super high flux microfiltration based on electrospun nanofibrous m-aramid membranes for water treatment. *Macromol. Res.* **23**, 601–606 (2015).
58. Zeng, P., Wang, K., Falkenstein-Smith, R. & Ahn, J. Effects of sintering temperature on the performance of SrSc0.1Co0.9O3-δ oxygen semipermeable membrane. *Braz. J. Chem. Eng.* **32**, 757–765 (2015).
59. Kayvani Fard, A. *et al.* Inorganic membranes: Preparation and application for water treatment and desalination. *Materials* **11**, 74 (2018).
60. Eom, J.-H., Kim, Y.-W. & Song, I.-H. Processing of kaolin-based microfiltration membranes. *J. Korean Ceram. Soc.* **50**, 341–347. https://doi.org/10.4191/kcers.2013.50.5.341 (2013).
61. Azeez, F. *et al.* The effect of surface charge on photocatalytic degradation of methylene blue dye using chargeable titania nanoparticles. *Sci. Rep.* **8**, 7104 (2018).
62. Al Ruqaishy, M. *et al.* Template-free preparation of TiO_2 microspheres for the photocatalytic degradation of organic dyes. *Korean J. Chem. Eng.* **35**, 2283–2289. https://doi.org/10.1007/s11814-018-0122-9 (2018).
63. Huo, P. *et al.* Photocatalytic degradation of antibiotics in water using metal ion@ TiO_2/HNTs under visible light. *Desalin. Water Treat.* **52**, 6985–6995 (2014).
64. Wali, Q., Bakr, Z. H., Manshor, N. A., Fakharuddin, A. & Jose, R. SnO2–TiO_2 hybrid nanofibers for efficient dye-sensitized solar cells. *Sol. Energy* **132**, 395–404 (2016).
65. Chen, H. *Tissue Engineering Approach Using Fibrous Scaffold with Matricellular Protein for Wound Healing* (2018).
66. Lakshmi, S., Renganathan, R. & Fujita, S. Study on TiO_2-mediated photocatalytic degradation of methylene blue. *J. Photochem. Photobiol., A* **88**, 163–167 (1995).
67. Lee, J., Ha, J.-H. & Song, I.-H. Improving the antifouling properties of ceramic membranes via chemical grafting of organosilanes. *Sep. Sci. Technol.* **51**, 2420–2428 (2016).
68. Banerjee, S., Dionysiou, D. D. & Pillai, S. C. Self-cleaning applications of TiO_2 by photo-induced hydrophilicity and photocatalysis. *Appl. Catal. B* **176**, 396–428 (2015).
69. Xing, M. *et al.* Super-hydrophobic fluorination mesoporous MCF/TiO_2 composite as a high-performance photocatalyst. *J. Catal.* **294**, 37–46 (2012).
70. Xu, X., Zhong, W., Zhou, S., Trajtman, A. & Alfa, M. Electrospun PEG–PLA nanofibrous membrane for sustained release of hydrophilic antibiotics. *J. Appl. Polym. Sci.* **118**, 588–595 (2010).
71. Lee, J., Ha, J.-H. & Song, I.-H. Enhanced fouling resistance of surface-modified alumina membranes by controlling humic acid and negatively charged-organosilane concentrations. *Desalin. Water Treat.* **88**, 16–24 (2017).
72. Selvam, S. & Sarkar, I. Bile salt induced solubilization of methylene blue: Study on methylene blue fluorescence properties and molecular mechanics calculation. *J. Pharm. Anal.* **7**, 71–75 (2017).
73. Kaur, N., Shahi, S. K. & Singh, V. Anomalous behavior of visible light active TiO_2 for the photocatalytic degradation of different Reactive dyes. *Photochem. Photobiol. Sci.* **14**, 2024–2034 (2015).
74. Vinu, R., Akki, S. U. & Madras, G. Investigation of dye functional group on the photocatalytic degradation of dyes by nano-TiO_2. *J. Hazard. Mater.* **176**, 765–773 (2010).
75. Zhu, X.-D., Wang, Y.-J., Sun, R.-J. & Zhou, D.-M. Photocatalytic degradation of tetracycline in aqueous solution by nanosized TiO_2. *Chemosphere* **92**, 925–932 (2013).

76. Houas, A. *et al.* Photocatalytic degradation pathway of methylene blue in water. *Appl. Catal. B* **31**, 145–157 (2001).
77. Lindsey, M. E. & Tarr, M. A. Inhibition of hydroxyl radical reaction with aromatics by dissolved natural organic matter. *Environ. Sci. Technol.* **34**, 444–449 (2000).
78. Teixeira, S. *et al.* Photocatalytic degradation of recalcitrant micropollutants by reusable $Fe_3O_4/SiO_2/TiO_2$ particles. *J. Photochem. Photobiol. A* **345**, 27–35 (2017).
79. Davies, E., Lowe, A., Sterns, M., Fujihara, K. & Ramakrishna, S. Phase morphology in electrospun zirconia microfibers. *J. Am. Ceram. Soc.* **91**, 1115–1120 (2008).
80. Li, D., Frey, M. W. & Joo, Y. L. Characterization of nanofibrous membranes with capillary flow porometry. *J. Membr. Sci.* **286**, 104–114. https://doi.org/10.1016/j.memsci.2006.09.020 (2006).

Acknowledgements

This work was supported by (1) the Technology Innovation Program of the Ministry of Trade, Industry and Energy (Republic of Korea) [grant number 20003782]; and (2) the Research Program of the Korea Institute of Materials Science (Republic of Korea) [grant number PNK 6780].

Author contributions

J.Y.H. and J.L. both contributes equally to performing the experiment, analyzing the data and writing of the manuscript. The design of the experiments was performed by J.L. (corresponding author) who is in charge of the research project. S.Z.A.B., J.-H.H. and I.-H.S. conducted some experiments (ex. TiO_2 coating and membrane performance test) jointly and participated in the collection and processing of experimental results.

Competing interests

The authors declare no competing interests.

Additional information

Supplementary information is available for this paper at https://doi.org/10.1038/s41598-020-74637-1.

Correspondence and requests for materials should be addressed to J.L.

Reprints and permissions information is available at www.nature.com/reprints.

Publisher's note Springer Nature remains neutral with regard to jurisdictional claims in published maps and institutional affiliations.